

How Shells of Different Shapes Affect Current-Driven Sand Transport

Kooistra, Tjitske J.; Haarbosch, Steven H.; Bosma, Jorn W.; Bouma, Tjeerd J.; van Prooijen, Bram C.; Soetaert, Karline; Pearson, Stuart G.

DOI

[10.1029/2025JC023346](https://doi.org/10.1029/2025JC023346)

Publication date

2025

Document Version

Final published version

Published in

JRG Oceans

Citation (APA)

Kooistra, T. J., Haarbosch, S. H., Bosma, J. W., Bouma, T. J., van Prooijen, B. C., Soetaert, K., & Pearson, S. G. (2025). How Shells of Different Shapes Affect Current-Driven Sand Transport. *JRG Oceans*, 130(11), Article e2025JC023346. <https://doi.org/10.1029/2025JC023346>

Important note

To cite this publication, please use the final published version (if applicable).
Please check the document version above.

Copyright

Other than for strictly personal use, it is not permitted to download, forward or distribute the text or part of it, without the consent of the author(s) and/or copyright holder(s), unless the work is under an open content license such as Creative Commons.

Takedown policy

Please contact us and provide details if you believe this document breaches copyrights.
We will remove access to the work immediately and investigate your claim.

How Shells of Different Shapes Affect Current-Driven Sand Transport



Key Points:

- Sandy seabeds with shells require higher depth-averaged flows for initiation of motion of the sand than a bare sandy seabed
- Both round and elongated shells decrease bedload transport of sand up to 50%
- The shape of the shell determines the effect on bed roughness and armoring of sand

Supporting Information:

Supporting Information may be found in the online version of this article.

Correspondence to:

S. G. Pearson,
s.g.pearson@tudelft.nl

Citation:





Kooistra, T. J., Haarbosch, S. H., Bosma, J. W., Bouma, T. J., van Prooijen, B. C., Soetaert, K., & Pearson, S. G. (2025). How shells of different shapes affect current-driven sand transport. *Journal of Geophysical Research: Oceans*, 130, e2025JC023346. <https://doi.org/10.1029/2025JC023346>

Received 21 AUG 2025

Accepted 27 OCT 2025

Author Contributions:

Conceptualization: Tjitske J. Kooistra, Jorn W. Bosma, Tjeerd J. Bouma, Karline Soetaert, Stuart G. Pearson
Data curation: Tjitske J. Kooistra, Steven H. Haarbosch, Jorn W. Bosma
Formal analysis: Tjitske J. Kooistra, Steven H. Haarbosch, Jorn W. Bosma
Funding acquisition: Bram C. van Prooijen, Stuart G. Pearson
Investigation: Tjitske J. Kooistra, Steven H. Haarbosch, Jorn W. Bosma
Methodology: Tjitske J. Kooistra, Steven H. Haarbosch, Jorn W. Bosma, Stuart G. Pearson
Project administration: Tjitske J. Kooistra, Jorn W. Bosma
Resources: Tjeerd J. Bouma

Tjitske J. Kooistra¹ , Steven H. Haarbosch² , Jorn W. Bosma³ , Tjeerd J. Bouma^{1,3} , Bram C. van Prooijen² , Karline Soetaert^{1,4} , and Stuart G. Pearson² 

¹Department of Estuarine and Delta Systems, Royal Netherlands Institute for Sea Research, Yerseke, The Netherlands,

²Faculty of Civil Engineering & Geosciences, Delft University of Technology, Delft, The Netherlands, ³Department of Physical Geography, Faculty of Geosciences, Utrecht University, Utrecht, The Netherlands, ⁴Department of Earth Sciences, Faculty of Geosciences, Utrecht University, Utrecht, The Netherlands

Abstract The seabed rarely consists solely of bare sand: often other materials, such as shells are present. They can influence sand transport by armoring the bed and modifying its roughness. Biogenic shells come in different shapes and sizes, depending on the mollusc species that produce them. To understand how changes in bivalve species composition affect sediment transport, we need a mechanistic understanding of how shell content and shell shape influence the near-bed flow and sand transport. We performed experiments in a racetrack flume, testing the effect of elongated (*Ensis leei*) versus rounded (*Spisula subtruncata*) shells on unidirectional current-driven sand transport. For both types of shells, a higher depth-averaged flow velocity was needed for initiation of motion and a decrease in bedload transport of sand was found. At a shell content of 20%, the threshold of motion of sand increased up to 75%, and bedload transport was reduced by up to 50%. These effects are explained by a balance between roughness-induced turbulence and bed armoring. Compared to a bare bed, shells decreased bed roughness by reducing ripple formation; rounded shells lowered roughness more than elongated shells, which formed roughness elements themselves, but also covered a larger fraction of the bed. However, there was no clear difference between round versus elongated shells on the overall sand transport; only shell content was key for the overall effect. Our results imply that sediment transport is likely overpredicted when a high number of shells is present in the seabed.

Plain Language Summary On sandy sea bottoms, empty shells are often present. They remain in the sand long after the animal that lived in the shell has died. These shells can influence how water currents move sand over the seafloor. Some shells are rounded while others are elongated, and they might influence the transport in different ways. We performed experiments in a flume, a laboratory channel in which a tray with sand and shells was placed, and in which the water current was controlled. We found that both types of shells made it harder for sand to start moving and also reduced how much sand moved in total. Shells made the bed smoother overall, leaving fewer sand ripples. Both shell types had a similar overall effect on sand movement, so the amount of shells in the sand was more important than the shape of the shells. The implications of the study are that we might currently be overestimating how much sand moves when a lot of shells are present in the seabed.

1. Introduction

Carbonate shells produced by molluscs remain in the sediment long after the animal has died and can persist over geological timescales (Gutiérrez et al., 2003; Kidwell & Jablonski, 1983). In highly productive areas, such as intertidal flats, the yearly shell production is typically more than 100 g m⁻² (Beukema & Cadée, 1999). Because of both high production and durability, shells can occupy a substantial fraction (up to 60%) of the sediment volume and regularly cover considerable parts of the seabed in shallow coastal areas (Kidwell & Jablonski, 1983; van der Spek et al., 2022). By adding these persistent structures to the sediment, bivalves can be considered long-term ecosystem engineers (Gutiérrez et al., 2003).

The shell deposits in the top layers of the sediment usually originate from locally occurring species (Al-Dabbas & McManus, 1987; van der Spek et al., 2022). Changes in the mollusc community, for instance through biological invasions, can therefore affect the composition of the shell mixture in the surface sediment. An example is the Atlantic razor clam (*Ensis leei*), which was introduced in Western Europe in the 1970s, and has become dominant in terms of biomass and abundance within the first 30 years of its invasion (Dekker & Beukema, 2012; Tulp

© 2025. The Author(s).

This is an open access article under the terms of the [Creative Commons Attribution License](https://creativecommons.org/licenses/by/4.0/), which permits use, distribution and reproduction in any medium, provided the original work is properly cited.

Supervision: Tjeerd J. Bouma, Bram C. van Prooijen, Karline Soetaert, Stuart G. Pearson

Visualization: Tjitske J. Kooistra, Steven H. Haarbosch

Writing – original draft: Tjitske J. Kooistra

Writing – review & editing: Tjitske J. Kooistra, Steven H. Haarbosch, J. W. Bosma, Tjeerd J. Bouma, Bram C. van Prooijen, Karline Soetaert, Stuart G. Pearson

et al., 2010). The elongated bivalve has taken this dominant position from the native cut through shell (*Spisula subtruncata*), characterized by its rounded shells. Ecologically, no significant negative effect of the *E. leei* invasion on *S. subtruncata* populations has been recorded, even though both species occur in the coastal zone (de Fouw et al., 2024; Dekker & Beukema, 2012). *E. leei* can reach population densities of hundreds of individuals per square meter (Witbaard et al., 2015), and is already one of the most prevalent shell types in North Sea coastal sediments. Their empty shells typically form large accumulations on beaches (Kerckhof et al., 2007; van der Spek et al., 2022), as well as on the seabed.

Although numerous studies have looked into the settling velocity, incipient motion, or transport of shells of different shapes (Al-Dabbas & McManus, 1987; Allen, 1984; Chen, Liu, et al., 2024; Dey, 2003; Diedericks et al., 2018; Fick, 2020; Fick et al., 2025; Kumagai & Nakajima, 2012; Li et al., 2020; Mehta et al., 1980; Miedema & Ramsdell, 2011; Ramsdell et al., 2011; Silva et al., 2023), up to date only a few studies investigated the effects of shells on the transportability and composition of the sediment they are embedded in. Shells have been shown to decrease ripple size, reduce ripple migration rates (Cheng et al., 2021) and stabilize sediments (Gutiérrez & Iribarne, 1999) under unidirectional flow, and shell fragments decrease bedload transport rates under oscillatory flow (Kumagai & Nakajima, 2012). Two main processes could underlie this influence on sediment transport: (a) alteration of the near-bed flow and turbulence and/or (b) armoring of the. Furthermore, in certain configurations, shells in the sediment promote the entrainment of silt in their wake (Pilditch et al., 1997; Witbaard et al., 2017).

Shells can form roughness elements which interact with the flow, comparable to other biogenic roughness elements, such as invertebrate tube structures (Borsje et al., 2009, 2011; Friedrichs et al., 2000, 2009) and vegetation stems (Bouma et al., 2007, 2009; Nepf, 2012). For these structures it has been found that they can on the one hand locally increase turbulence and create scouring and thereby promote sediment transport, and on the other hand, at a larger scale, cause skimming flow that protects the seabed (Borsje et al., 2009, 2011; Bouma et al., 2007, 2009). For vegetation, sediment transportability is driven by changes in turbulence level (Hendriks et al., 2008, 2010). Here, turbulent kinetic energy (k_t) predicts both the onset of sediment motion and the amount of bedload transport better than bed shear stress (Xu et al., 2022; Yang et al., 2016; Yang & Nepf, 2018; Zhao & Nepf, 2021). For shells, the interaction with the flow depends on their shape and positioning (Miedema & Ramsdell, 2011). Contrary to tubeworms and vegetation, shells are less likely to form vertical structures. Additionally, shells can decrease sand ripple formation and size, which decreases bed roughness and near-bed turbulence (Cheng et al., 2021).

Armoring occurs when the shear stress is above the erosion threshold for the fine fraction but below that of the coarse fraction. This causes a persistent coarse top layer, which shelters the lower layer and reduces further sediment transport (Little & Mayer, 1976; Wilcock & DeTemple, 2005). Shells have a higher erosion threshold compared to sand and are therefore suitable candidates for armoring (Miedema & Ramsdell, 2011; Ramsdell et al., 2011). On beaches, an armoring shell layer can form, reducing wind-driven transport of sand and stabilizing the bed (McKenna Neuman et al., 2012; van der Wal, 1998). Shells have already been incorporated into aeolian transport equations, which predict transport reasonably well (Strypsteen et al., 2021; van Rijn & Strypsteen, 2020). However, in aquatic environments like the seafloor or river beds, such transport equations are still lacking due to limited experimental studies quantifying shell-effects on hydrodynamic-driven sediment transport. In this study, we conducted a flume experiment as a first step toward quantifying how shells of different shapes influence current-driven sand transport.

To date, only very few studies have touched upon the effect of shells or shell fragments on erodibility and transport of sand by hydrodynamic forcing (Cheng et al., 2021; Gutiérrez & Iribarne, 1999; Kumagai & Nakajima, 2012). The impact of shells has however not yet been quantified in terms of transport rates. This quantification is needed for the implementation of shell-content effects in sediment transport models. Furthermore, the diversity in shell shapes complicates making uniform predictions. If the shape of a shell determines its effect on sediment transport, a change in the morphology of the bivalve community could drive changes in the long-term bioengineering effects of their shells. The research questions we aim to answer are therefore: (a) how do elongated and round shells affect incipient motion and bedload transport rates of sand, and (b) what is the balance between increased transport through roughness and turbulence versus decreased transport through armoring? We hypothesize that shells decrease the transportability of sand through the process of armoring, but that elongated shells create roughness elements which may interact more strongly with the flow. To investigate this, we performed laboratory flume

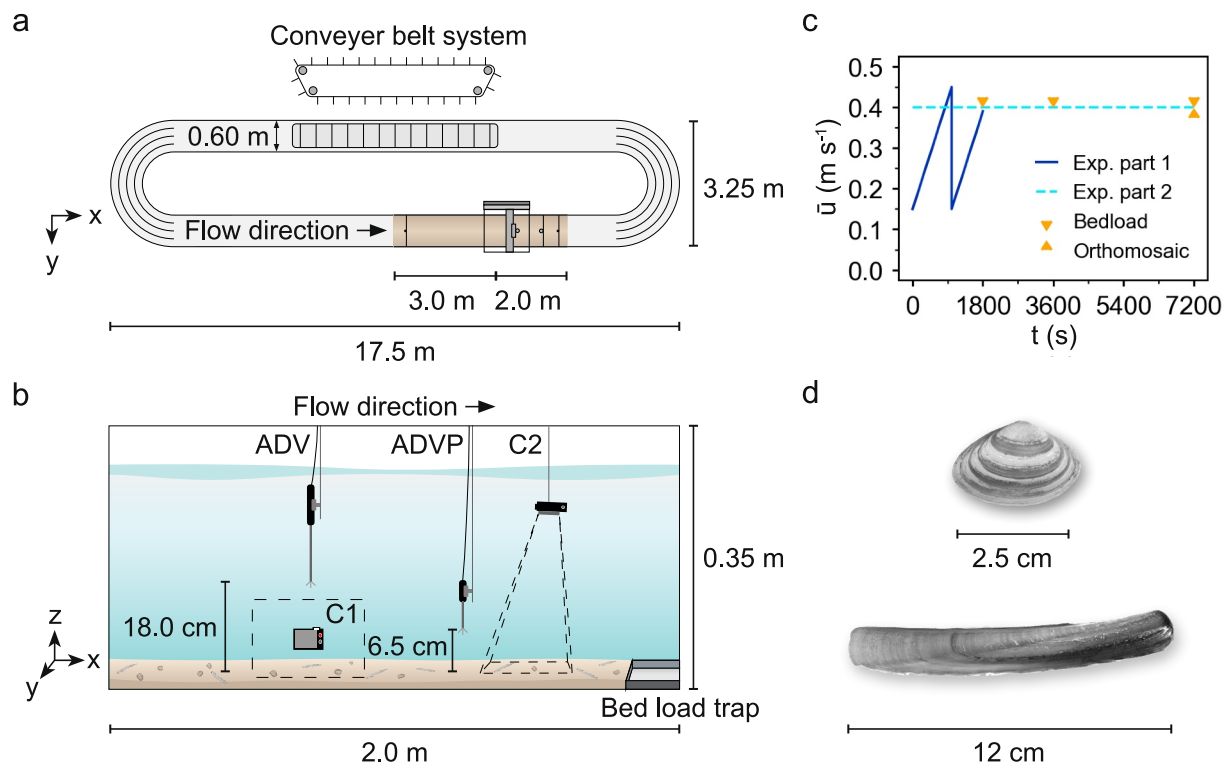


Figure 1. Flume set-up and experimental runs: (a) top view of the racetrack flume with the conveyor belt (top), and supply- and test section (brown, bottom right); (b) side view of the 2-m test section with positioning of instruments (ADV, ADVP), cameras (side view camera C1, and top-view camera C2) and bedload trap; (c) schematic representation of flow velocity settings during experimental runs: Part 1 (threshold of motion) with two stages of accelerating flow, Part 2 (bedload transport) with constant flow, and time points of sampling bedload and taking orthomosaic pictures in the Part 2 experiments; (d) pictures of the two bivalve species shells used: *Spisula subtruncata* (top) and *Ensis leei* (bottom).

experiments on artificial beds of sand mixed with shells from elongated bivalve *Ensis leei* or rounded *Spisula subtruncata*. We explain incipient motion and bedload transport by roughness creation and surface cover. The results from this study can be used as building blocks for improving existing sand transport models. Furthermore, we gain a better understanding of the bioengineering of the diverse types of bivalve shells.

2. Materials and Methods

2.1. Experimental Set-Up

The experiments were performed in a racetrack flume, located at NIOZ Royal Netherlands Institute for Sea Research in Yerseke (Bouma et al., 2005; Jonsson et al., 2006). The oval flume is 17.5 m long and 3.25 m wide, with a flow channel width of 0.6 m (Figure 1a). A conveyor belt system on one of the straight sides of the flume creates unidirectional current velocities up to $u = 0.6 \text{ m s}^{-1}$. At the end of the opposite straight side, a 2-m long test section with a glass viewing window is located (Figure 1b). The flume was filled with tap water to a depth of 0.35 m and brought to a salinity of 30 ppm by adding sea salt. We measured salinity prior to every run using a salinity tester (HI98319, Hanna Instruments). Average water temperature was 12.5°C.

For measuring current velocity at the test section, we used a Vectrino Acoustic Doppler Velocimeter (ADV, Nortek AS), mounted on a 3D positioning system. The ADV probe was placed approximately halfway along the test bed in the center of the flume (Figure 1b), measuring current velocity at 25 Hz, at a level of $0.37 \times$ total water depth (h) above the bed, to obtain depth-averaged velocity (\bar{u}), assuming a logarithmic flow profile (Kleinhans, 2005). The experimental set-up also included a Vectrino Profiler (ADVP, Nortek AS), measuring the near-bed velocity profile downstream of the ADV. Due to technical problems, we were not able to acquire profile data from all the experimental runs. For all available data and runs, see Table S2 in Supporting Information S1.

We recorded the bed mobility and surface development with two cameras (HERO4 Session, GoPro). The side view camera was mounted outside the window of the test section, at the position of the ADV, and the top view camera was mounted just below the water level, downstream of the ADVP, so that minimal interaction with the measurements and near-bed flow occurred. In addition, to monitor the evolution of the bed surface, we captured a set of top-view photos (GoPro HERO4 Silver) of the bed surface over the complete length of the test section at intervals of 5 cm. Ground Control Points (GCPs) were placed on the flume bottom and sides at the start and end of the test section, and on the walls in the middle of the test section. This configuration allowed for the automated stitching of multiple photos into a single orthomosaic (see Section 2.4.5). All cameras were set to a linear field of view, to minimize lens distortion.

2.2. Bed Composition

For the sediment mixture, siliciclastic North Sea sand ($d_{50} = 0.348$ mm; $d_{90} = 0.525$ mm) with a density of 2640 kg m^{-3} was used. The grain size composition was measured by laser diffraction (Mastersizer 2000, Malvern Instruments) and the density was tested with a pycnometer. Empty shells of *Ensis leei* and *Spisula subtruncata* (from here on referred to as *Ensis* and *Spisula*, Figure 1d) were acquired from a shell-processing factory (Meromar Seafoods, Harlingen, Netherlands) and cleaned with enzyme-based detergent. Morphological characteristics of the shells are presented in table S1 of Supporting Information S1. We tested sediments with *Ensis*, *Spisula* or a mix of both, in the following bulk volumetric shell contents (P_{shell}): 0% (bare sand), 10% and 20%, for each shell type or a mix of both types. Besides whole shells, we added shell fragments (4 L for every 10 L bulk shell volume) to mimic a natural sand-shell mixture. These shell contents lie within the range found in coastal environments (see Section 4.5). The sand and the desired bulk volume of shells were mixed in a standing cement mixer and added to the sediment tray. The dimensions ($L \times W \times H$) of the trays were $160.5 \times 57.5 \times 25.5$ cm, with a false bottom, leaving the total depth of the sediment at 12 cm. The tray was lifted into the test section, with a lifting crane and the edges were filled with foam strips to prevent the space between the tray edge and the flume walls from becoming a sediment sink. After placing the tray in the flume, several buckets of sediment mixture were added on top of the test bed, so that the surface of the bed was just above the edges of the tray, after compaction. Prior to each experimental run, we re-mixed the sediment and flattened it by raking to ensure that the following run began with a random bed. We covered the flume bottom 3 m upstream of the test section with a thin (± 3 cm) layer of the experimental sediment-shell mixture. This was to ensure that the test bed was not supply limited and allow the flow to adjust prior to reaching the test section.

2.3. Experimental Runs

Two types of experimental runs were performed: (a) an accelerating flow experiment to determine the threshold of motion, and (b) a constant flow experiment to determine bedload transport rates. For an overview of all experimental runs and settings, see Table S2 in Supporting Information S1.

2.3.1. Part 1: Threshold of Motion

To determine the depth-averaged velocity at the threshold of motion of sand grains, we performed initial experimental runs with slowly accelerating flow (Figure 1c). The starting current velocity \bar{u} of each run was 0.15 m s^{-1} , increasing by approximately $0.02 \text{ m s}^{-1} \text{ min}^{-1}$ until we observed full bed mobility. Next, \bar{u} was again linearly increased over time, starting from 0.15 m s^{-1} , to test the critical velocity for a water-worked bed, that is, a bed that has an organized roughness structure created by the streamflow. After the initial analysis, we used the threshold of motion observed during the second acceleration, on a water-worked bed. This gives a more realistic observation, for in nature we rarely find a bed that has been flattened or has not been water-worked. Each experimental run took approximately 30 min.

We identified the current velocity at the first motion stage as defined by Breusers and Schukking (1971) and van Rijn (1984): a few rolling grains. For this, we manually determined the onset of incipient motion of sand grains, visual from side and top-view video footage, while using the live observations of initiation of grain movement as a reference point.

2.3.2. Part 2: Bedload Transport

To quantify the bedload transport, we performed experimental runs with a constant current velocity for 2 hr (Figure 1c). The tested current velocities ranged from 0.25 to 0.45 m s⁻¹. Since we expected shells to affect turbulence and thus transport, the lowest constant velocity was set near the critical velocity, $\bar{u}_{\text{crit}} \approx 0.3 \text{ m s}^{-1}$, as determined in Part 1.

The transported sediment was collected in a bedload trap (58.5 × 20.0 × 12.0 cm), located at the end of the test section. The current was interrupted to empty the bedload trap after 30, 60, and 120 min—the end of the run. Bedload samples were dried at 60°C for 8–10 days, then sieved over a 1-mm sieve to separately weigh the coarse (shell) and the fine (sand) fraction, which we summed to acquire the total bedload mass.

2.4. Data Analysis

The raw data and code to execute the analysis is available in Kooistra et al. (2025).

2.4.1. Current Velocity Data Processing

We filtered the ADV velocity time-series for correlation values >70% and a signal-to-noise ratio >10 dB (Nortek A.S., 2022). After several sensitivity tests, we identified these thresholds to maximize the amount of data kept without affecting the outcomes because of low quality data. Next, we de-spiked the velocity time series applying two filters: (a) a difference filter between two consecutive measurements of 0.5 m s⁻¹, and (b) a threshold filter ($0 < u < 0.7 \text{ m s}^{-1}$; $-0.2 < v < 0.2 \text{ m s}^{-1}$; and $-0.1 < w < 0.1 \text{ m s}^{-1}$). For the depth-averaged velocity \bar{u} in Part 1 (threshold of motion), we used the median of the measured depth-averaged velocities from the ADV measurements over the 10 s preceding and the 10 s following the identified motion stage. The selection of a 20-s window was short enough to prevent the filtering out of large turbulent fluctuations, while still being long enough to obtain an accurate velocity measurement. For \bar{u} in experiment Part 2 (bedload transport) we used the mean of the filtered velocity data over each sampling interval (mean and standard deviations of \bar{u} can be found in Table S3 of Supporting Information S1).

2.4.2. Near-Bed Velocity and Turbulence

We measured near-bed profiles for six experimental runs from the bedload transport experiment (Table S2 in Supporting Information S1). For the data processing of the ADVP, we applied similar quality control criteria as with the ADV data: correlation value >70%, a signal-to-noise ratio of >10 dB. Furthermore, we set a minimum amplitude of -40 dB and applied again a difference filter between two consecutive u , v or w measurements of 0.5 m s⁻¹. We selected a 5-min time window approximately halfway the experimental run, during which the bottom level was constant and corrected the height of the measurement points by the mean value of the detected bottom level.

To check whether the near-bed current velocity followed a logarithmic profile, we fitted a linear regression to u (ADVP measurements) over $\ln(z)$, by a constrained least squares regression fixed at \bar{u} (ADV measurement). Next, we derived shear velocity u^* following the “law of the wall”:

$$\bar{u} = \frac{u_*}{\kappa} \ln \frac{z}{z_0} \quad (1)$$

In which u^* is the shear velocity, κ is the Von Karman constant ($\kappa \approx 0.41$) and z_0 is the roughness height. This shear velocity u^* allowed us to compare the skin friction coefficient c_f of shelly versus bare beds:

$$c_f = \left(\frac{u_*}{\bar{u}} \right)^2 \quad (2)$$

The standard deviation of the velocity fluctuations relative to the mean gave the turbulence intensity (u' , v' , w'). From this, we determined turbulent kinetic energy (k_t) near the bed (Soulsby, 1983):

$$k_t = \frac{1}{2} (u'^2 + v'^2 + w'^2) \quad (3)$$

The dimensionless turbulent kinetic energy (k_t^*) is given by:

$$k_t^* = \frac{k_t}{\left(\frac{\rho_s}{\rho_w} - 1\right) g d_{50}} \quad (4)$$

in which the sediment density $\rho_s = 2,640 \text{ kg m}^{-3}$, water density $\rho_w = 1,027 \text{ kg m}^{-3}$ (at 10°C and a salinity of 30 ppt) and gravitational acceleration $g = 9.81 \text{ m s}^{-2}$.

2.4.3. Bed Shear Stress and Friction

The water flow exerts a shear stress on the bed surface. This grain bed shear stress (τ , N m^{-2}) is directly correlated with bed roughness (van Rijn, 1993):

$$\tau = \rho_w g \frac{\bar{u}^2}{C^2} \quad (5)$$

with the Chézy roughness C , given by the White-Colebrook formula:

$$C = 18 \times \log 10 \left(\frac{12R}{k_{s,\text{grain}}} \right) \quad (6)$$

in which R is the hydraulic radius $R = 0.16 \text{ m}$ (calculated with the height of the water column and the width of the flume), and grain roughness $k_{s,\text{grain}} = 2 \times d_{90} = 1.05 \times 10^{-3} \text{ m}$ (Kamphuis, 2010).

The dimensionless bed shear stress, or Shields number, can be calculated based on the bed shear stress (van Rijn, 1984):

$$\theta = \frac{\tau}{(\rho_s - \rho_w) g d_{50}} \quad (7)$$

2.4.4. Bedload Transport

The sediment mass transport rate is computed for each sampling interval by:

$$q = \frac{m_{\text{sed}}}{W \Delta t} \quad (8)$$

with sediment mass transport rate q ($\text{kg m}^{-1} \text{ s}^{-1}$), determined by total dry weight of the transported sediment (m_{sed}) divided by the width (w) of the flume during each sampled time window (Δt). This can be converted to a non-dimensional bedload transport rate φ , or Einstein parameter:

$$\varphi = \frac{q_s}{\rho_s w_s d_{50}} \quad (9)$$

with settling velocity $w_s = 0.046 \text{ m s}^{-1}$, following van Rijn (1993) Equation 3.2.22 for non-spherical particles $100 < d_{50} < 1,000 \text{ }\mu\text{m}$. This dimensionless sediment transport rate is commonly related to the bed shear stress or Shields number (θ):

$$\varphi = m(\alpha_i \theta - \theta_{\text{critical}})^{1.5}, \text{ with } \alpha_i = \frac{\theta_{\text{critical},i\%}}{\theta_{\text{critical},0\%}} \quad (10)$$

with no transport occurring when $\theta < \theta_{\text{critical}}$. This relation was originally formulated by Meyer-Peter and Müller (1948) (hereafter referred to as MPM), with the critical Shields number defining the onset of sediment motion, $\theta_{\text{critical}} = 0.047$, a scale factor $m = 8$, and with $\alpha_i = 1$. A reanalysis of this formulation by Wong and Parker (2006) (hereafter referred to as WP) showed slightly different values: $\theta_{\text{critical}} = 0.0495$ and $m = 3.97$. The model parameters from MPM and WP were based on experiments with featureless bed conditions and uniform sediments, with fully mobile transport conditions (Meyer-Peter & Müller, 1948; Wong & Parker, 2006). In contrast, our experiments contained bedforms and shells and were conducted using low flow velocities. Therefore, the values of the bedload model coefficients were expected to differ. To account for the effects of the shells on shear stress, we introduce a factor α , which indicates the ratio between the real shear stress (in case of shells) and the shear stress in case for a bare sand bed (no shells). We determine this factor α by determining for which depth-averaged flow velocity sand starts moving for the situation with and without shells in Part 1 of the experiment. We emphasize here that the shells change the turbulence and thereby the bed shear stress, and not the initiation of motion of a sand particle. We optimized fitting parameter m using non-linear least square regression (NLS). For this fitting, we selected the data above $\theta_{\text{critical}} = \theta_{\text{critical},0\%} = 0.0423$, as obtained from Part 1. As starting parameter, the WP parameter was used ($m = 3.97$), and θ_{critical} was set as $\theta_{\text{critical},0\%} = 0.0423$.

2.4.5. Roughness and Armoring

For the bed surface structure analysis, we used the top-view orthomosaic images taken after 120 min of constant flow (Part 2). We used Agisoft Metashape Professional (v. 2.1.3, Agisoft LLC) to create detailed 3D models based on the Structure from Motion (SfM) technique (Westoby et al., 2012). First, a series of images were loaded into the workspace, with low-quality images removed manually. GCP marker data, measured with an approximated accuracy of 5 mm relative to a fixed local 3D coordinate system, was also uploaded; the coordinate system's origin was set at the center of the test bed at the level of the flume bottom. GCPs were identified automatically, followed by a manual check. Next, we generated a sparse point cloud with automated image alignment, which was refined through calibration using the GCP data and optimizing all selectable camera parameters, including additional corrective fits. A dense point cloud was then generated with mild depth filtering. Using this dense point cloud, a Digital Surface Model (DSM) was constructed through planar projection, and an orthomosaic was created based on the DSM. Finally, a bounding box with coordinates $[-0.6, -0.2; 0.6, 0.2]$ was applied to both the DSM and orthomosaic, which were then exported at a spatial resolution of 0.001 m, resulting in images with dimensions of $1,200 \times 400$ pixels each. We determined the areal coverage of shells by manually outlining the shells visible in the orthomosaics using ImageJ. Based on these contours a mask was created and the relative areal cover (%) was calculated (Figure S1 in Supporting Information S1). To avoid capturing side-wall effects on bed roughness, we selected our area of interest as the middle region (0.8 m in x -direction and 0.4 m in y -direction). Roughness was determined as the elevation range of a focal area, that is, the difference between the minimum and maximum elevation (Wilson et al., 2007), using the package “terra” in R (Hijmans, 2020; R Core Team, 2024). We selected a focal area of 11×11 pixels to approximate the scale of shells and sand ripples (0.01 m). Total bed roughness ($k_{s,\text{bed}}$, m) was then calculated as the mean roughness over the entire area of interest.

3. Results

3.1. Threshold of Motion

The presence of shells increased the critical depth-averaged velocity and critical Shields at incipient motion in a water-worked bed (Figure 2). A higher shell content lead to a higher $\bar{u}_{\text{critical}}$ for initiation of motion of sand grains: from $\bar{u}_{\text{critical}} = 0.28 \text{ m s}^{-1}$ and $\theta_{\text{critical}} = 0.042$ at a bare bed to $\bar{u}_{\text{critical}}$ ranging between 0.32 and 0.36 m s^{-1} and θ_{critical} between 0.057 and 0.071 at $P_{\text{shell}} = 20\%$. Shell content P_{shell} rather than shell morphology was the driving factor: both elongated as well as round shells resulted in a similar order of magnitude increase in $\bar{u}_{\text{critical}}$ and θ_{critical} .

3.2. Near-Bed Velocity and Turbulence

The near-bed current velocity (u ; m s^{-1}) approached a logarithmic profile (r^2 ranged between 0.78 and 0.94; Figure 3a). The presence of shells resulted in lower c_f values compared to bare beds under comparable flow conditions. Near-bed turbulence (k_t^*) was higher on bare beds than on beds with shells under comparable depth-

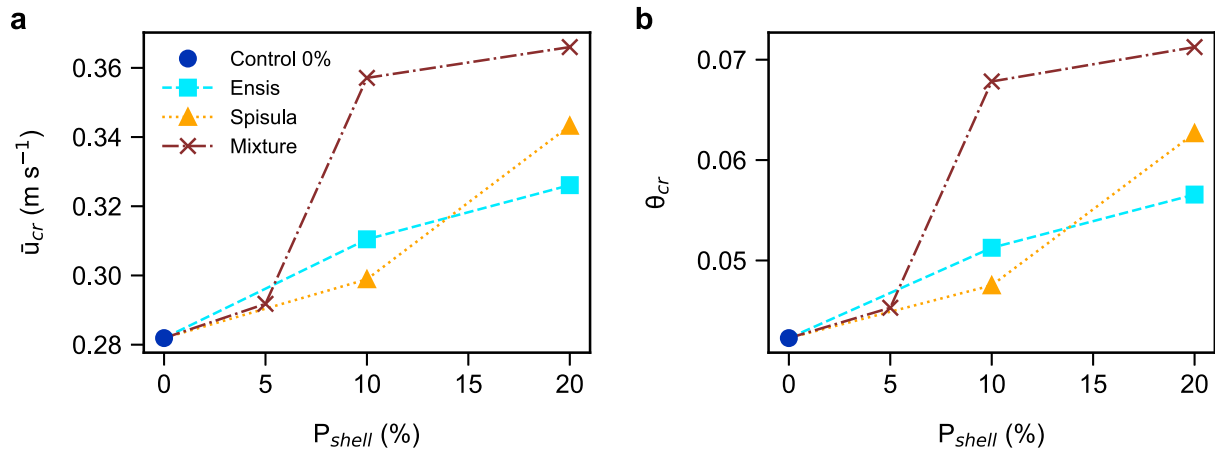


Figure 2. (a) Depth-averaged current velocity and (b) critical Shields parameter at the incipient motion of sand grains for different sand-shell bed compositions.

averaged flow (Figure 3b). For some of the shelly beds, k_t^* displayed a peak between 0.5 and 1 cm from the bed ($z/h = 0.01$ – 0.04 ; Figure 3b).

3.3. Bedload Transport: Comparing Measurements to Literature Predictions

Bedload transport was lower when shells were present, while a higher shell content resulted in a greater reduction of bedload transport (Figure 4a). At $P_{shell} = 20\%$ and $\bar{u} = \bar{u}_{max}$, the amount of sand transported was reduced by approximately 50%. At $P_{shell} = 10\%$, the reduction in transport was less pronounced and at $\bar{u} = \bar{u}_{max}$ transport rates approached those of a bare bed. Similar as in Part 1, there was no clear difference in the effect of the two different shell types. At the lowest current velocities, near the threshold of motion, bedload transport was close to zero in both bare and shelly beds.

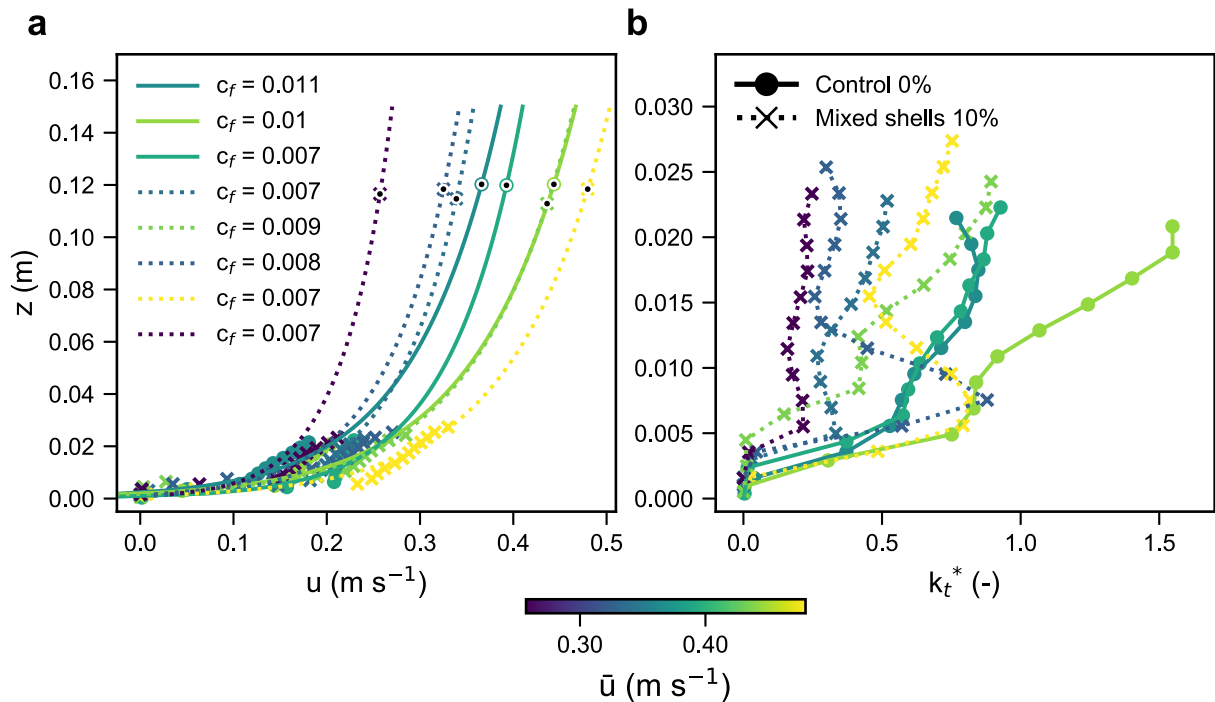


Figure 3. Profiles for the bedload transport experiments (Part 2, constant flow), for bare beds (round markers, solid line) and beds containing 10% mixed shells (x-markers, dotted line). Plot color indicates the mean depth-averaged velocity, with brighter colors indicating higher flow velocity. (a) Near-bed velocity u and logarithmic profiles fitted to all velocity measurements (near-bed u and \bar{u} , calculated c_f values are displayed); (b) near-bed turbulence k_t^* .

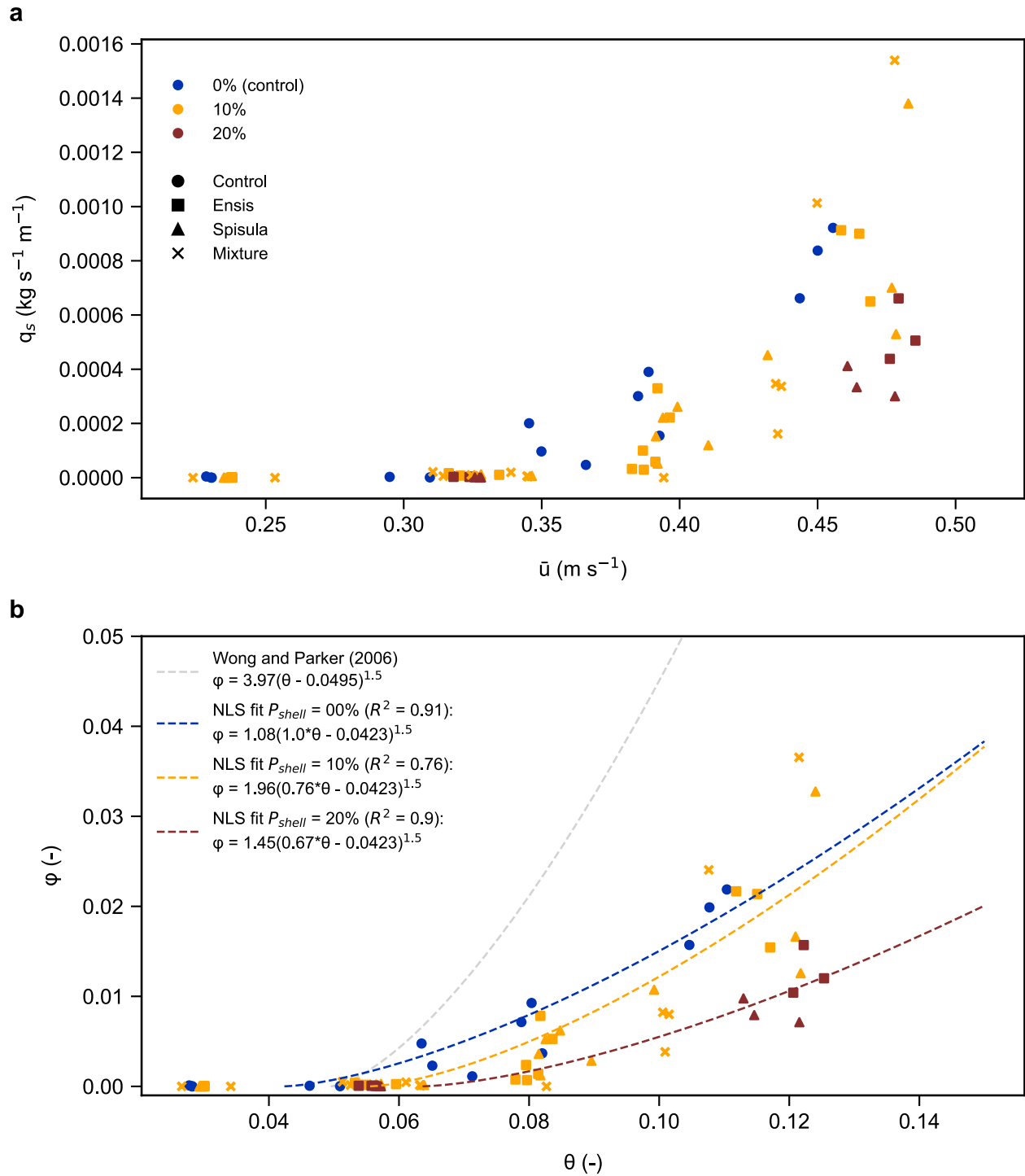


Figure 4. (a) Bedload transport flux at different current velocities for all tested bed configurations and (b) dimensionless bedload transport rate (ϕ) over dimensionless grain bed shear stress, or Shields (θ). Plotted lines describe the best-fit bedload models for each shell content (0%, 10%, and 20%). The predictor with parameters from Wong and Parker (2006) ($\theta_{critical} = 0.0495$ and $m = 3.97$) is displayed in grey.

The theoretical WP relations between ϕ and θ overestimated the transported bedload (Figure 4b). For bare beds as well as sand with shells, the optimized scale parameter m was lower than the value given by Wong and Parker (2006). The bare bed resulted in the lowest value ($m = 1.08$), whereas shells increased m ($m = 1.96$ for $P_{shell} = 10\%$ and $m = 1.45$ for $P_{shell} = 20\%$). Parameter α , which was set to account for the shell effect on θ as

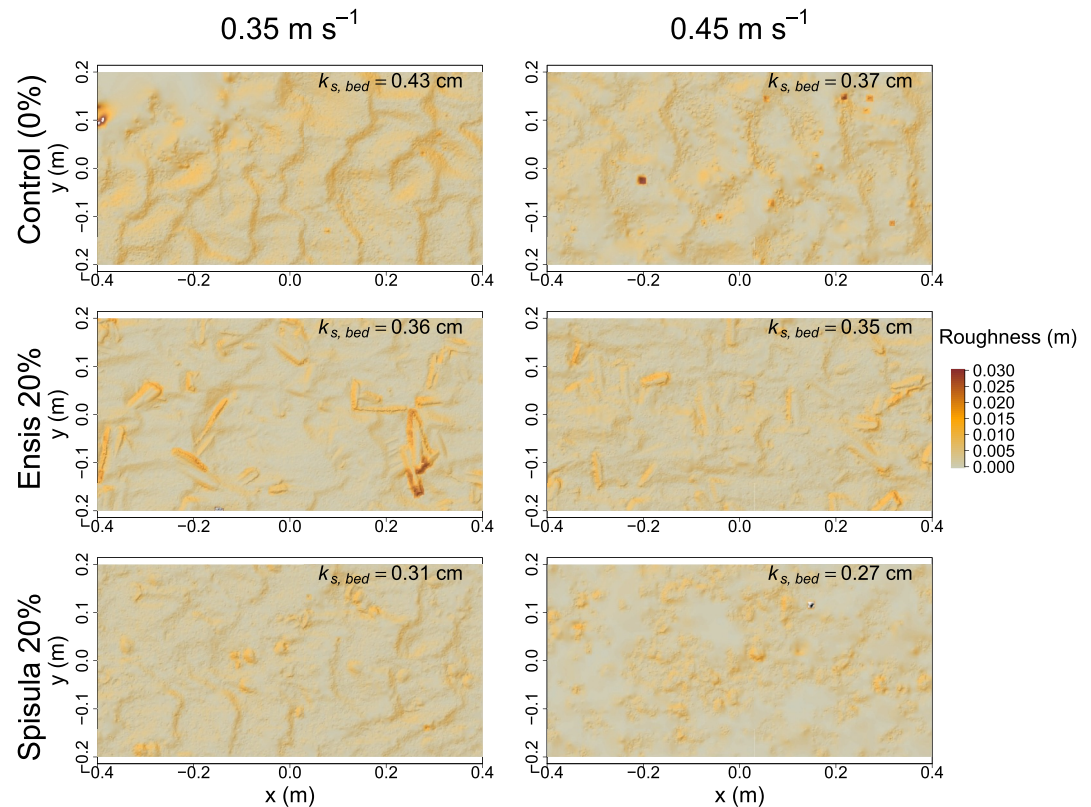


Figure 5. Three example digital surface models (DSMs) after 2 hr of constant flow (0.35 or 0.45 m s^{-1}) for beds containing 0% shells, 20% *Ensis* or 20% *Spisula* shells. Note that the color scale was capped at 0.03 m to increase the visibility of smaller roughness elements.

determined in Part 1, captured most of the decrease in transport with increasing shell content ($\alpha_{10\%} = 0.76$ and $\alpha_{20\%} = 0.67$). For 10% shells, a steeper curve and hence a higher m was then required to capture the high transport rates at \bar{u}_{\max} . For 20% shells, due to the strongly decreased transport rates at \bar{u}_{\max} , less steepening was needed and therefore a lower m sufficed.

3.4. Total Bed Roughness and Areal Coverage

The sand ripples that increase total roughness of the bed without shells largely disappeared when shells are present (Figure 5). Total bed roughness $k_{s,\text{bed}}$ decreased with increasing shell content (Figure 6a). Bare beds and beds with *Ensis* shells resulted in the highest roughness ($k_{s,\text{bed}} = 0.35\text{--}0.43 \text{ cm}$), while *Spisula* shells resulted in the lowest roughness ($k_{s,\text{bed}} = 0.27\text{--}0.37 \text{ cm}$) (Figure 6a). *Ensis* shells themselves form large roughness elements, whereas *Spisula* shells form minimal roughness elements. In terms of areal cover, *Ensis* shells covered a larger fraction of the bed compared to *Spisula* shells at $P_{\text{shell}} = 20\%$ (Figure 6b).

4. Discussion

Shells increased the velocity and shear stress at the onset of sediment motion and decreased the bedload transport of sand. While at 10% shell content, transport was only reduced at lower flow velocities, at higher (e.g., 20%) shell content, bedload transport was halved compared to a bare sand bed. This reduction is independent of shell morphology, although shell shape does determine how much the shells interact with bed morphology and hydrodynamics. Both shell types decreased roughness by decreasing ripple formation, but elongated shells formed large roughness elements themselves and thereby lowered total bed roughness to a lesser extent than rounded shells. However, as the elongated shells covered a larger areal fraction of the bed, they sheltered a larger amount of the sediment from near-bed flow compared to rounded shells. These counteracting effects on roughness and bed cover resulted in a similar decrease in sediment transport between shell types (Figure 7).

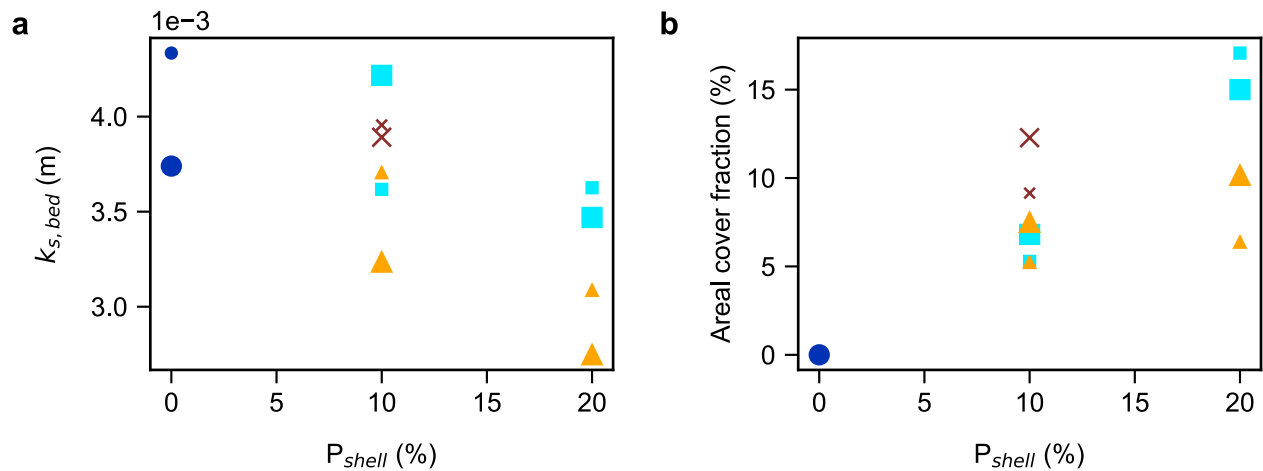


Figure 6. (a) Total bed roughness $k_{s,bed}$, and (b) areal cover fraction of the comparable constant flow experiments (smaller marker: 0.35 m s^{-1} ; larger marker: 0.45 m s^{-1}) for beds containing 0% shells (dot), 10% mixed (x), *Ensis* (square) or *Spisula* (triangle) shells and 20% *Ensis* or *Spisula* shells. Labels for shell types as in Figure 2.

4.1. Shells Increased the Threshold of Motion

Contrary to our findings, Cheng et al. (2021) observed a decrease in the threshold of motion ($u_{critical}$) and the critical shear stress ($\theta_{critical}$) up to a shell content of 20%. This could be explained by the fact that we determined incipient motion on a water-reworked rippled bed as would be found in nature, while they looked at an initial, only theoretically existing, flat bed. In our experiment, shells decreased the threshold of motion in some initial beds as

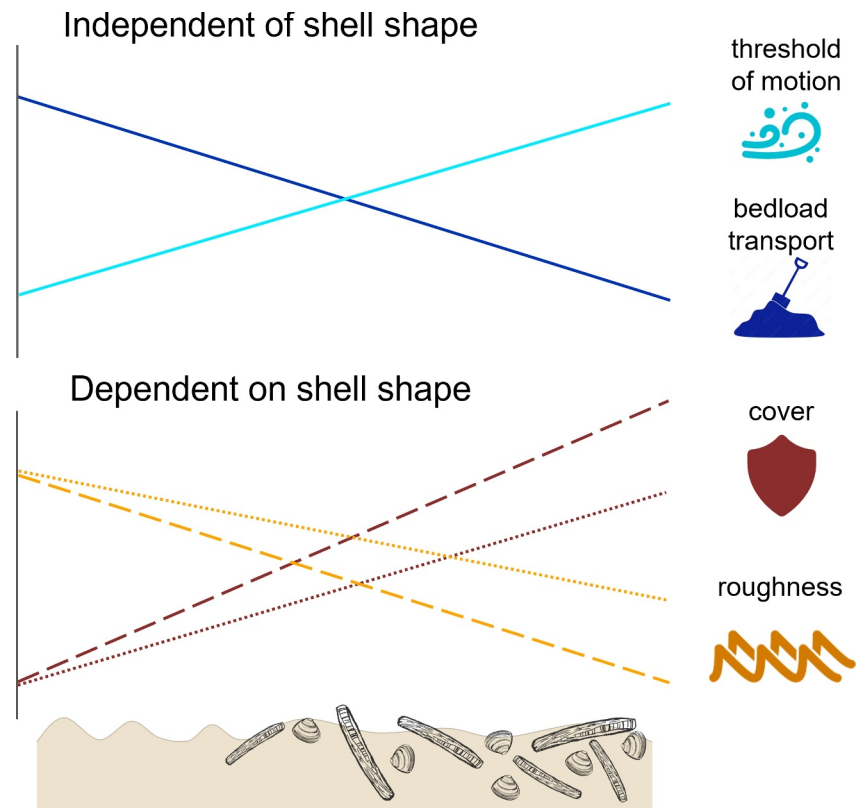


Figure 7. Schematic overview of observed effects of shells on threshold of motion and bedload transport, through bed cover and diminishing roughness. Dashed lines indicate *Ensis*, dotted lines *Spisula*, solid lines indicate effects independent of shell shape.

well, however, we considered the water-worked bed to be more representative of a natural reference situation. In heterogeneous sand-gravel mixtures, the θ_{critical} of sand with 20% gravel was in the same order of magnitude as our value of θ_{critical} at $P_{\text{shell}} = 20\%$ by McCarron et al. (2019). They attributed this to hiding-exposure effects, a mechanism that plays a role in sand-shell mixtures as well. Furthermore, including factor α in the bedload prediction to represent the effect of shells on θ_{critical} , largely accounted for the decrease in sediment transport at higher shell contents.

4.2. What Happened Close to the Bed?

Shells decreased the skin friction coefficient c_f , which is consistent with our findings that shelly beds are less rough than rippled ones. This is also in line with field measurements above rippled sand beds and shelly beds, as summarized in Soulsby (1983): $c_f = 0.0024$ for a sand/shell bed, and $c_f = 0.0061$ for rippled sand. These values lie slightly below the range that we found (0.007–0.01), which might be attributed to the difference in measurement elevation (1 m above the bottom) and field versus experimental context.

Shells decrease near-bed turbulence compared to a bare bed (Figure 4b). This corresponds to previous observations of lowered near-bed turbulence in the presence of 10% shells (Cheng et al., 2021) or gravel clusters (Curran & Tan, 2014). Although our 10% mixed shelly beds, had similar roughness values to the bare bed, shells were distributed in patches, while ripples regularly covered the bare bed (Figure 5). This could partly explain the differential effect on turbulence, as the shape and spacing of roughness elements play a role in the magnitude of near-bed turbulence (McKenna Neuman et al., 2012). Cheng et al. (2021) saw near-bed turbulence increase for higher shell contents. Therefore, a greater shell content than measured in the current experiment may increase turbulence to a similar level as above the bare bed. Based on our measurements on total bed roughness, we expect the threshold above which shells increase turbulence to depend on shell morphology, and to be lower for round shells compared to elongated shells.

4.3. Reduction of Bedload Transport: Magnitude and Mechanisms

At the highest shell content (20%), bedload transport was approximately halved compared to a sandy bed without shells. This decrease approaches the 75% decrease in ripple migration rate measured by Cheng et al. (2021), at slightly higher current velocities (0.5 m s^{-1}). Extrapolating our findings to higher current velocities would likely result in an even larger difference in transported bedload between shelly and bare beds. Furthermore, since transported sand grains do not always maintain contact with the bed, but can also move by saltation and in suspension (van Rijn, 1984), the ripple migration rate as used in Cheng et al. (2021) might underestimate bedload transport. The decrease in bedload transport over shelly beds is consistent with field observations of decrease in sand transport when the seafloor consists of a mix of fine sand with shells, compared to bare sand (Pickrill, 1986).

Both in the bare and shelly beds, we observed an overestimation of bedload transport by the Wong and Parker (WP) bedload predictor. Several factors could explain this mismatch. Firstly, the WP parameters were defined for a featureless bed. On rippled beds, the WP parameters have been previously observed to be inaccurate (Guevara et al., 2024). Secondly, the original parameters were developed for fully mobile conditions and have been shown to overestimate transport at low velocities (Kleinhans & van Rijn, 2002; Ribberink, 1998). In heterogeneous sediments, this could be attributed to the hindrance of small grain movement by larger grains and can be corrected with a hindrance factor (Kleinhans & van Rijn, 2002). In our study, different shell shapes and sizes complicated the formulation of a single factor based on particle dimensions. Rather we chose to fit the m -parameter (Equation 10) directly, after accounting for the effect of shells on the threshold of motion by means of a factor α . The decreasing α with shell content captured the decrease in bedload transport by shells compared to bare sand. The fitted m -parameter was always lower than the WP value (3.97), but was lowest for bare sand (1.08) and highest for beds with 10% shells (1.96). This increased value for m was required to steepen the curve and capture both the lower transport near the threshold of motion as well as the high transport at high flow velocity. These results are consistent with Jumars and Nowell (1984), who note that the impact of benthos on sediment transport rates tends to decrease at higher sediment transport rates. Sediment transport in beds with 20% shells remained below bare-bed transport rates within the tested velocity range, leading to a less steep curve slope and therefore an intermediate fit for m (1.45). Overall, these results suggest that $P_{\text{shell}} = 20\%$ substantially decreases sediment transport, while $P_{\text{shell}} = 10\%$ might lie below certain thresholds for areal cover or roughness to limit transport at higher flow velocities, analogous to previously identified roughness density thresholds (Bouma et al., 2009; Friedrichs

et al., 2009; Nowell & Church, 1979). This threshold could be attributed to a transition from isolated roughness flow to a skimming flow regime.

4.4. Shells can Modify Roughness and Shield Sand

Shells diminished sand ripples and consequently decreased bed roughness. This confirms the findings from Cheng et al. (2021). Additionally, we saw that the elongated shells reduce roughness to a lesser extent than rounded shells, as elongated shells form roughness elements themselves. This corresponds with a higher drag for particles with a lower shape factor (Chen, Yao, et al., 2024; Li et al., 2020), as the shape factor of elongated shells was 0.12, compared with 0.30 for round shells (Table S1 in Supporting Information S1). Furthermore, at $P_{\text{shell}} = 10\%$, the total roughness of beds, whether with elongated or mixed shells, still fall within the range of bare beds. Contrarily, Cheng et al. (2021) measured minimal roughness based on near-bed turbulence at $P_{\text{shell}} = 10\%$, above which bed roughness increased. Although our DSM-based method may contain biases, for instance, due to dependence on the raster resolution (Wilson et al., 2007), we attempted to correct for this by selecting a suitable scale. Rather than a value derived from local flow conditions, our DSM-based roughness gives a direct measure of the roughness for the entire bed, that is, at the macroscale level. The lower c_f values for shelly beds also agree with the lower roughness, even though we only have c_f measurements for 10% mixed shells. The decreased roughness could be responsible for the increase in threshold of motion: sediment is less readily entrained due to a decrease in turbulent bursts.

In sediments with armoring, bedload transport is overestimated by the original bedload models (Hunziker & Jaeggi, 2002). During our 2-hr experimental runs, the top layer of the sediment did not coarsen (Table S4 in Supporting Information S1), possibly due to sufficient upstream sediment supply, nor did the transport rate decrease over time. Shells, however, covered up to 15% of the bed for elongated *Ensis* shells, and 8%–10% for the same bulk volume content of rounded *Spisula* shells. In aeolian settings, shells have been shown to limit sand transport already from low shell contents. A 20% shell content reduced the amount of transported sand by up to 80% (van der Wal, 1998). This reduction of sediment transport is of the same order of magnitude as our measured bedload transport effects. Bed cover by shells resulted in stabilization of the sand surface in wind tunnel experiments, resulting in an up to 45% increase of the threshold of motion (McKenna Neuman et al., 2012), which is similar to our observed increase in the threshold of motion. In line with our findings, large shells here also resulted in higher cover fractions than small shells.

As a next step, a shell reduction factor such as the Bagnold equation for aeolian transport (van Rijn & Stryptsteen, 2020), could be defined for transport equations in aquatic settings. Alternatively, the m and α parameters can be adapted directly within a MPM-like bedload predictor, following the results of this study. To increase the accuracy of these parameters, we recommend testing a wider range of shell contents and flow conditions. This would also increase the applicability in a wider range of field conditions.

4.5. Outlook and Applications

Before upscaling our findings, a few limitations should be considered. Firstly, we tested current velocities up to 0.45 m s^{-1} , in the lower transport stage (as defined by van Rijn (1993)). Tidal currents velocities of 1 m s^{-1} are common in the coastal zone (Elias et al., 2022). Although we observed some mobility, most of our shells remained in place even during the faster flow conditions. With stronger currents, however, they may be swept away. Secondly, we tested unimodal, sandy sediment, while different interactions may be at play when mud is present. The effect of shells in cohesive sediments remains therefore to be considered in future experiments.

The shell contents used in this study fall within the range of shell contents measured in the field (Figure 8) and previously reported (Wells & Kim, 1989). Shell distribution is however heterogeneous. To implement shells in sediment transport models, data sets with a higher resolution of sediment shell content are needed. Hydroacoustic mapping could provide such an increased resolution, compared to sediment sampling (Mielck et al., 2014).

Elongated and round shells had similar effects on sediment transport, even if their interaction with bedforms and their areal coverage of the bed differs. Therefore, the replacement of a native by an invasive species with a different shell morphology will likely not directly affect the sediment transportability. However, when shell production in an area increases, for instance, because an invasive species has a higher abundance or can colonize habitats that were previously less occupied by similar-sized bivalves, this might have implications for sediment

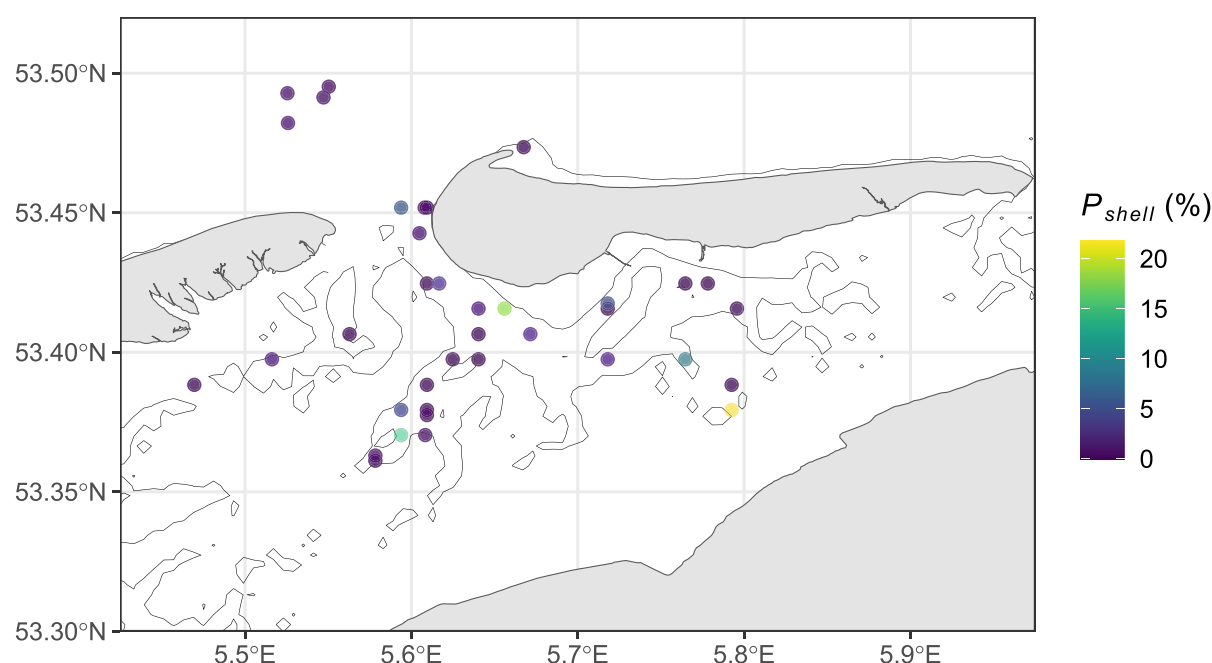


Figure 8. Volumetric shell contents measured near the Ameland inlet, Wadden Sea, the Netherlands. Note that shell content here was measured as water-replacement volume, and is therefore likely lower than the bulk volume used in the current study. The sampling methodology is described in Text S1 of Supporting Information S1.

transport processes. *Ensis leei* has been suggested to colonize previously “empty” habitats because of its resilience to hydrodynamic stress (Dekker & Beukema, 2012). Additionally, to date, there is no evidence that this species has replaced native species. Therefore, the large increase in shell production by the colonization of *Ensis leei* might have had an effect on sediment transport.

By decreasing sediment transportability, shells may feedback into larger-scale morphological processes, such as sand wave formation and migration. Biogeomorphological effects have previously been implemented in models for sand wave occurrence and morphology (Borsje et al., 2009; Damveld et al., 2020). Additionally, including coarser fractions improved modeled sand wave migration rates (Z. Wang et al., 2019). Given the prevalence of shells in shallow marine basins, incorporating biogeomorphological effects could lead to more accurate predictions of sand wave development. Another problem in morphodynamic modeling is the overestimation of channel incision, which is usually calibrated by modifying bed roughness, increasing sediment grain size or increasing the transverse slope parameter to unrealistic values (Baar et al., 2019; Y. Wang et al., 2016). Shells are prevalent in these deeper gullies, and including them might therefore improve predictions of channel incision. Lastly, including shells in sediment nourishments may improve the durability of the nourishment (Strypsteen et al., 2021). The empirical results from our study could serve to predict the effects of shells in the distribution of the nourished sediment. The ecological effects of such applications should however not be neglected (Peterson et al., 2014).

5. Conclusions

Shells increase the shear stress at threshold of motion and decrease the bedload transport of sand. The magnitude of these effects is similar for different shell shapes, even though the underlying mechanisms—such as the formation of roughness elements and the spatial coverage by shells—vary depending on shell shape. Given the widespread occurrence of shells in marine sediments, these significant effects likely have implications for large-scale sediment transport predictions. By redefining parameters in sediment transport formulations to account for the presence of shells, we made a step toward including their influence in sediment transport models. This knowledge contributes to more realistic forecasting of sediment dynamics.

Appendix A: List of Symbols

The definitions and (if applicable) units of the symbols used in this paper are given below.

α_i	ratio between $\theta_{\text{critical},0\%}$ and $\theta_{\text{critical},i\%}$ [–]
C	Chézy roughness [$\text{m}^{1/2} \text{s}^{-1}$]
c_f	skin friction coefficient [–]
$d_{50}; d_{90}$	median grain size; 90th percentile of cumulative grain size distribution [mm]
g	gravitational acceleration [9.81 m s^{-2}]
$\theta; \theta_{\text{critical}}$	dimensionless bed shear stress, or Shields number; critical Shields number [–]
$k_s; k_{s,\text{bed}}$	roughness; total bed roughness [m]
$k_t; k_t^*$	turbulent kinetic energy [$\text{m}^2 \text{s}^{-2}$]; dimensionless turbulent kinetic energy [–]
κ	Von Karman constant ($\kappa \approx 0.41$)
m	scale parameter in MPM-like bedload predictor
P_{shell}	shell content [%]
q_s	sediment mass transport rate [$\text{kg s}^{-1} \text{m}^{-1}$]
$\rho_s; \rho_w$	sediment density; water density [kg m^{-3}]
R	hydraulic radius [m]
τ	bed shear stress [N m^{-2}]
\bar{u}	depth-averaged velocity in x -direction [m s^{-1}]
$u'; v'; w'$	turbulence intensity in x , y and z direction [m s^{-1}]
u^*	shear velocity [m s^{-1}]
ϕ	dimensionless bedload transport rate (or Einstein parameter) [–]
w_s	settling velocity [m s^{-1}]
z	height above bed [m]
z_0	roughness length [m]

Acknowledgments

We would like to thank Chiu Cheng, Jaco de Smit and Timothy Price for their involvement in the initial advice and brainstorming during conceptualisation, and troubleshooting during the experiment and analysis. Thanks to Lennart van IJzerloo, André den Herder and Arne den Toonder for practical assistance with the flume set-up and Peter van Breugel for analyzing sediment samples. We thank André Seinen from Meromar Seafoods for saving up *Ensis* and *Spisula* shells. Furthermore, we would like to thank Maarten Kleinhans, Gerben Ruessink and Sierd de Vries for their advice and feedback on the methodology and analysis and Rob Witbaard for feedback on the draft manuscript. Funding for this study was provided by NWO Grant 17600: “Tracking Ameland Inlet Living Lab Sediment (TRAILS)” and NWO Grant 18035: “Effective Upgrades and Retrofits for Coastal Climate Adaptation (EURECCA).” Additionally, Stuart Pearson received funding from NWO Grant 21026: “Revealing Hidden Networks of Coastal Sediment Pathways.”

Conflict of Interest

The authors declare no conflicts of interest relevant to this study.

Data Availability Statement

The ADV and ADVP data, sediment data, and images for determining the initiation of motion, flow characteristics, bed characteristics and bedload transport rates in the study are available at the NIOZ Dataverse via <https://doi.org/10.25850/nioz/7b.b.0j> with CC0 access (Kooistra et al., 2025).

Python and *R* code used for data processing, analyses and creating the figures in this paper is preserved at the NIOZ Dataverse via <https://doi.org/10.25850/nioz/7b.b.0j> with CC0 access (Kooistra et al., 2025).

References

- Al-Dabbas, M. A. M., & McManus, J. (1987). Shell fragments as indicators of bed sediment transport in the Tay Estuary. *Proceedings of the Royal Society of Edinburgh. Section B. Biological Sciences*, 92(3–4), 335–344. <https://doi.org/10.1017/s0269727000004759>
- Allen, J. R. L. (1984). Experiments on the settling, overturning and entrainment of bivalve shells and related models. *Sedimentology*, 31(2), 227–250. <https://doi.org/10.1111/j.1365-3091.1984.tb01961.x>

- Baar, A. W., Boechat Albernaz, M., van Dijk, W. M., & Kleinhans, M. G. (2019). Critical dependence of morphodynamic models of fluvial and tidal systems on empirical downslope sediment transport. *Nature Communications*, 10(1), 1–12. <https://doi.org/10.1038/s41467-019-12753-x>
- Beukema, J. J., & Cadée, G. C. (1999). An estimate of the sustainable rate of shell extraction from the Dutch Wadden Sea. *Journal of Applied Ecology*, 36(1), 49–58. <https://doi.org/10.1046/j.1365-2664.1999.00380.x>
- Borsje, B. W., Hulscher, S. J. M. H., Herman, P. M. J., & De Vries, M. B. (2009). On the parameterization of biological influences on offshore sand wave dynamics. *Ocean Dynamics*, 59(5), 659–670. <https://doi.org/10.1007/s10236-009-0199-0>
- Borsje, B. W., Kruijt, M., der Werf, J. V., Hulscher, S., & Herman, P. (2011). Modeling biogeomorphological interactions in underwater nourishments. *Coastal Engineering Proceedings*, 1(32), 104. <https://doi.org/10.9753/icce.v32.sediment.104>
- Bouma, T. J., De Vries, M. B., Low, E., Peralta, G., Tanczos, I. C., Van De Koppel, J., & Herman, P. M. J. (2005). Trade-offs related to ecosystem engineering: A case study on stiffness of emerging macrophytes. *Ecology*, 86(8), 2187–2199. <https://doi.org/10.1890/04-1588>
- Bouma, T. J., Friedrichs, M., Van Wesenbeeck, B. K., Temmerman, S., Graf, G., & Herman, P. M. J. (2009). Density-dependent linkage of scale-dependent feedbacks: A flume study on the intertidal macrophyte *Spartina anglica*. *Oikos*, 118(2), 260–268. <https://doi.org/10.1111/j.1600-0706.2008.16892.x>
- Bouma, T. J., van Duren, L. A., Temmerman, S., Claverie, T., Blanco-García, A., Ysebaert, T., & Herman, P. M. J. (2007). Spatial flow and sedimentation patterns within patches of epibenthic structures: Combining field, flume and modelling experiments. *Continental Shelf Research*, 27(8), 1020–1045. <https://doi.org/10.1016/j.csr.2005.12.019>
- Breusers, H., & Schukking, W. (1971). *Begin Van beweging Van bodemmateriaal*. Delft Hydraulics.
- Chen, J., Liu, J., Jiang, C., Wu, Z., Yao, Z., & Bian, C. (2024). Incipient motion of single shells under currents in flume experiments. *Journal of Marine Science and Engineering*, 12(5), 820. <https://doi.org/10.3390/jmse12050820>
- Chen, J., Yao, Z., He, F., Jiang, C., Jiang, C., Wu, Z., et al. (2024). Experimental study on the settling motion of coral grains in still water. *Journal of Fluid Mechanics*, 990, A15. <https://doi.org/10.1017/jfm.2024.469>
- Cheng, C. H., de Smit, J. C., Fivash, G. S., Hulscher, S. J. M. H., Borsje, B. W., & Soetaert, K. (2021). Sediment shell-content diminishes current-driven sand ripple development and migration. *Earth Surface Dynamics*, 9(5), 1335–1346. <https://doi.org/10.5194/esurf-9-1335-2021>
- Curran, J. C., & Tan, L. (2014). Effect of bed sand content on the turbulent flows associated with clusters on an armored gravel bed surface. *Journal of Hydraulic Engineering*, 140(2), 137–148. [https://doi.org/10.1061/\(asce\)hy.1943-7900.0000810](https://doi.org/10.1061/(asce)hy.1943-7900.0000810)
- Damveld, J. H., Borsje, B. W., Roos, P. C., & Hulscher, S. J. M. H. (2020). Biogeomorphology in the marine landscape: Modelling the feedbacks between patches of the polychaete worm *Lanice conchilega* and tidal sand waves. *Earth Surface Processes and Landforms*, 45(11), 2572–2587. <https://doi.org/10.1002/esp.4914>
- de Fouw, J., van Horsen, P. W., Craeymeersch, J., Leopold, M. F., Perdon, J., Troost, K., et al. (2024). Spatio-temporal analysis of potential factors explaining fluctuations in population size of *Spisula subtruncata* in the Dutch North Sea. *Frontiers in Marine Science*, 11, 1476223. <https://doi.org/10.3389/fmars.2024.1476223>
- Dekker, R., & Beukema, J. J. (2012). Long-term dynamics and productivity of a successful invader: The first three decades of the bivalve *Ensis directus* in the western Wadden Sea. *Journal of Sea Research*, 71, 31–40. <https://doi.org/10.1016/j.seares.2012.04.004>
- Dey, S. (2003). Incipient motion of bivalve shells on sand beds. *Journal of Engineering Mechanics*, 129(2), 232–240. [https://doi.org/10.1061/\(asce\)0733-9399\(2003\)129:2\(232\)](https://doi.org/10.1061/(asce)0733-9399(2003)129:2(232))
- Diedericks, G. P. J., Troch, C. N. A., & Smit, G. J. F. (2018). Incipient motion of shells and shell gravel. *Journal of Hydraulic Engineering*, 144(3), 06017030. [https://doi.org/10.1061/\(asce\)hy.1943-7900.0001421](https://doi.org/10.1061/(asce)hy.1943-7900.0001421)
- Elias, E. P. L., Pearson, S. G., van der Spek, A. J. F., & Pluis, S. (2022). Understanding meso-scale processes at a mixed-energy tidal inlet: Ameland Inlet, the Netherlands – Implications for coastal maintenance. *Ocean & Coastal Management*, 222, 106125. <https://doi.org/10.1016/j.ocecoaman.2022.106125>
- Fick, C., Favoreto, J., Borghi, L., Puhl, E., Toldo, E. E., Neves, F. A. P. S., et al. (2025). Sedimentological and biofabric patterns for hybrid coquina deposits: Insights from wave tank experiments. *Sedimentology*, 72(6), 1992–2024. <https://doi.org/10.1111/sed.70028>
- Fick, C., Puhl, E., & Toldo, E. E., Jr. (2020). Threshold of motion of bivalve and gastropod shells under oscillatory flow in flume experiments. *Sedimentology*, 67(1), 627–648. <https://doi.org/10.1111/sed.12657>
- Friedrichs, M., Graf, G., & Springer, B. (2000). Skimming flow induced over a simulated polychaete tube lawn at low population densities. *Marine Ecology Progress Series*, 192, 219–228. <https://doi.org/10.3354/meps192219>
- Friedrichs, M., Leipe, T., Peine, F., & Graf, G. (2009). Impact of macrozoobenthic structures on near-bed sediment fluxes. *Journal of Marine Systems*, 75(3–4), 336–347. <https://doi.org/10.1016/j.jmarsys.2006.12.006>
- Guevara, O., Guan, L., Salinas, J. S., Zgheib, N., & Balachandrar, S. (2024). Sediment transport on rippled beds. *Physics of Fluids*, 36(11), 113339. <https://doi.org/10.1063/5.0236116>
- Gutiérrez, J. L., & Iribarne, O. (1999). Role of Holocene beds of the stout razor clam *Tagelus plebeius* in structuring present benthic communities. *Marine Ecology Progress Series*, 185, 213–228. <https://doi.org/10.3354/meps185213>
- Gutiérrez, J. L., Jones, C. G., Strayer, D. L., & Iribarne, O. O. (2003). Mollusks as ecosystem engineers: The role of shell production in aquatic habitats. *Oikos*, 101(1), 79–90. <https://doi.org/10.1034/j.1600-0706.2003.12322.x>
- Hendriks, I. E., Bouma, T. J., Morris, E. P., & Duarte, C. M. (2010). Effects of seagrasses and algae of the *Caulerpa* family on hydrodynamics and particle-trapping rates. *Marine Biology*, 157(3), 473–481. <https://doi.org/10.1007/s00227-009-1333-8>
- Hendriks, I. E., Sintes, T., Bouma, T. J., & Duarte, C. M. (2008). Experimental assessment and modeling evaluation of the effects of the seagrass *Posidonia oceanica* on flow and particle trapping. *Marine Ecology Progress Series*, 356, 163–173. <https://doi.org/10.3354/meps07316>
- Hijmans, R. J. (2020). Terra: Spatial data analysis. In *CRAN: Contributed packages*. <https://doi.org/10.32614/CRAN.package.terra>
- Hunziker, R. P., & Jaeggi, M. N. R. (2002). Grain sorting processes. *Journal of Hydraulic Engineering*, 128(12), 1060–1068. [https://doi.org/10.1061/\(asce\)0733-9429\(2002\)128:12\(1060\)](https://doi.org/10.1061/(asce)0733-9429(2002)128:12(1060))
- Jonsson, P. R., Van Duren, L. A., Amielh, M., Asmus, R., Aspden, R. J., Daunys, D., et al. (2006). Making water flow: A comparison of the hydrodynamic characteristics of 12 different benthic biological flumes. *Aquatic Ecology*, 40(4), 409–438. <https://doi.org/10.1007/s10452-006-9049-z>
- Jumars, P. A., & Nowell, A. R. M. (1984). Effects of benthos on sediment transport: Difficulties with functional grouping. *Continental Shelf Research*, 3(2), 115–130. [https://doi.org/10.1016/0278-4343\(84\)90002-5](https://doi.org/10.1016/0278-4343(84)90002-5)
- Kamphuis, J. W. (2010). Determination of sand roughness for fixed beds. *Journal of Hydraulic Research*, 12(2), 193–203. <https://doi.org/10.1080/00221687409499737>
- Kerckhof, F., Haelters, J., & Gollasch, S. (2007). Alien species in the marine and brackish ecosystem: The situation in Belgian waters. *Aquatic Invasions*, 2(3), 243–257. <https://doi.org/10.3391/ai.2007.2.3.9>
- Kidwell, S. M., & Jablonski, D. (1983). Taphonomic feedback ecological consequences of shell accumulation. In *Biotic interactions in recent and fossil benthic communities* (pp. 195–248). Springer. https://doi.org/10.1007/978-1-4757-0740-3_5

- Kleinhans, M. G. (2005). Flow discharge and sediment transport models for estimating a minimum timescale of hydrological activity and channel and delta formation on Mars. *Journal of Geophysical Research*, 110(E12), 1–23. <https://doi.org/10.1029/2005JE002521>
- Kleinhans, M. G., & van Rijn, L. C. (2002). Stochastic prediction of sediment transport in sand-gravel bed Rivers. *Journal of Hydraulic Engineering*, 128(4), 412–425. [https://doi.org/10.1061/\(asce\)0733-9429\(2002\)128:4\(412\)](https://doi.org/10.1061/(asce)0733-9429(2002)128:4(412))
- Kooistra, T. J., Haarbosch, S. H., Bosma, J. W., Bouma, T. J., van Prooijen, B. C., Soetaert, K., & Pearson, S. G. (2025). How shells of different shapes affect current-driven sand transport [data and code]. *NIOZ dataverse*. <https://doi.org/10.25850/nioz/7b.b.0j>
- Kumagai, T., & Nakajima, S. (2012). Experimental study on bed load transport of shell fragment-mixed sand under waves. *The International Journal of Ocean and Climate Systems*, 3(2), 85–96. <https://doi.org/10.1260/1759-3131.3.2.85>
- Li, Y., Yu, Q., Gao, S., & Flemming, B. W. (2020). Settling velocity and drag coefficient of platy shell fragments. *Sedimentology*, 67(4), 2095–2110. <https://doi.org/10.1111/sed.12696>
- Little, W. C., & Mayer, P. G. (1976). Stability of channel beds by armouring. *Journal of the Hydraulics Division*, 102(11), 1647–1661. <https://doi.org/10.1061/jycej.0004651>
- McCarron, C. J., Van Landeghem, K. J. J., Baas, J. H., Amoudry, L. O., & Malarkey, J. (2019). The hiding-exposure effect revisited: A method to calculate the mobility of bimodal sediment mixtures. *Marine Geology*, 410, 22–31. <https://doi.org/10.1016/j.margeo.2018.12.001>
- McKenna Neuman, C., Li, B., & Nash, D. (2012). Micro-topographic analysis of shell pavements formed by Aeolian transport in a wind tunnel simulation. *Journal of Geophysical Research*, 117(F4). <https://doi.org/10.1029/2012JF002381>
- Mehta, A. J., Lee, J., & Christensen, B. A. (1980). Fall velocity of shells as coastal sediment. *Journal of the Hydraulics Division*, 106(11), 1727–1744. <https://doi.org/10.1061/jycej.0005554>
- Meyer-Peter, E., & Müller, R. (1948). Formulas for bed-load transport. In *Proceedings of the 2nd meeting of the International Association of Hydraulic Research*.
- Miedema, S. A., & Ramsdell, R. C. (2011). Hydraulic transport of sand/shell mixtures in relation with the critical velocity. *Terra et Aqua (English Edition)*, 122. Retrieved from <https://resolver.tudelft.nl/uuid:ebca7d4c-1db2-4d55-a8f0-b0740e67b6a0>
- Mielck, F., Hass, H. C., & Betzler, C. (2014). High-resolution hydroacoustic seafloor classification of sandy environments in the German Wadden Sea. *Journal of Coastal Research*, 298(6), 1107–1117. <https://doi.org/10.2112/jcoastres-d-12-00165.1>
- Nepf, H. M. (2012). Hydrodynamics of vegetated channels. *Journal of Hydraulic Research*, 50(3), 262–279. <https://doi.org/10.1080/00221686.2012.696559>
- Nortek, A. S. (2022). The comprehensive manual - Velocimeters. <https://support.nortekgroup.com/hc/en-us/articles/360029839351-The-Comprehensive-Manual-Velocimeters>
- Nowell, A. R. M., & Church, M. (1979). Turbulent flow in a depth-limited boundary layer. *Journal of Geophysical Research*, 84(C8), 4816–4824. <https://doi.org/10.1029/JC084iC08p04816>
- Peterson, C. H., Bishop, M. J., Anna, L. M. D., & Johnson, G. A. (2014). Multi-year persistence of beach habitat degradation from nourishment using coarse shelly sediments. *Science of the Total Environment*, 487, 481–492. <https://doi.org/10.1016/j.scitotenv.2014.04.046>
- Pickrill, R. A. (1986). Sediment pathways and transport rates through a tide-dominated entrance, Rangaunu Harbour, New Zealand. *Sedimentology*, 33(6), 887–898. <https://doi.org/10.1111/j.1365-3091.1986.tb00989.x>
- Pilditch, C. A., Emerson, C. W., & Grant, J. (1997). Effect of scallop shells and sediment grain size on phytoplankton flux to the bed. *Continental Shelf Research*, 17(15), 1869–1885. [https://doi.org/10.1016/S0278-4343\(97\)00050-2](https://doi.org/10.1016/S0278-4343(97)00050-2)
- Ramsdell, R. C., Miedema, S. A., & Talmon, A. M. (2011). Hydraulic transport of sand/shell mixtures. *Proceedings of the International Conference on Offshore Mechanics and Arctic Engineering - OMAE*, 6, 533–547. <https://doi.org/10.1115/OMAE2011-49695>
- R Core Team. (2024). *R: A Language and environment for statistical computing (4.4.1)*. R Foundation for Statistical Computing.
- Ribberink, J. S. (1998). Bed-load transport for steady flows and unsteady oscillatory flows. *Coastal Engineering*, 34(1–2), 59–82. [https://doi.org/10.1016/S0378-3839\(98\)00013-1](https://doi.org/10.1016/S0378-3839(98)00013-1)
- da Silva, F. R. S., de Borges, A. L. O., Toldo, E. E. Jr., Fick, C., Puhl, E., Oliveira, V. C. B., & da Cruz, F. E. G. (2023). Threshold of motion and orientation of bivalve shells under current flow. *Brazilian Journal of Geology*, 53(1), e20220080. <https://doi.org/10.1590/2317-4889202320220080>
- Soulsby, R. L. (1983). The bottom boundary layer of shelf seas. In *Elsevier oceanography series* (Vol. 35, pp. 189–266). Elsevier. [https://doi.org/10.1016/S0422-9894\(08\)70503-8](https://doi.org/10.1016/S0422-9894(08)70503-8)
- Strypsteen, G., van Rijn, L. C., Hoogland, M. D., Rauwoens, P., Fordeyn, J., Hijma, M. P., & Lodder, Q. J. (2021). Reducing Aeolian sand transport and beach erosion by using armour layer of coarse materials. *Coastal Engineering*, 166, 103871. <https://doi.org/10.1016/j.coastaleng.2021.103871>
- Tulp, I., Craeymeersch, J., Leopold, M., van Damme, C., Fey, F., & Verdaat, H. (2010). The role of the invasive bivalve *Ensis directus* as food source for fish and birds in the Dutch coastal zone. *Estuarine, Coastal and Shelf Science*, 90(3), 116–128. <https://doi.org/10.1016/j.ecss.2010.07.008>
- van der Spek, A., Forzoni, A., & Vermaas, T. (2022). Holocene deposits at the lower shoreface and inner shelf of the Dutch coast. *Ocean & Coastal Management*, 224, 106203. <https://doi.org/10.1016/j.ocecoaman.2022.106203>
- van der Wal, D. (1998). The impact of the grain-size distribution of nourishment sand on aeolian sand transport. *Journal of Coastal Research*, 14(2), 620–631. Retrieved from <https://www.jstor.org/stable/4298816>
- van Rijn, L. C. (1984). Sediment transport, part I: Bed load transport. *Journal of Hydraulic Engineering*, 110(10), 1431–1456. [https://doi.org/10.1061/\(asce\)0733-9429\(1984\)110:10\(1431\)](https://doi.org/10.1061/(asce)0733-9429(1984)110:10(1431))
- van Rijn, L. C. (1993). *Principles of sediment transport in rivers, estuaries and coastal seas*. Aqua Publications.
- van Rijn, L. C., & Strypsteen, G. (2020). A fully predictive model for aeolian sand transport. *Coastal Engineering*, 156, 103600. <https://doi.org/10.1016/j.coastaleng.2019.103600>
- Wang, Y., Yu, Q., Jiao, J., Tonnon, P. K., Wang, Z. B., & Gao, S. (2016). Coupling bedform roughness and sediment grain-size sorting in modelling of tidal inlet incision. *Marine Geology*, 381, 128–141. <https://doi.org/10.1016/j.margeo.2016.09.004>
- Wang, Z., Liang, B., Wu, G., & Borsje, B. W. (2019). Modeling the formation and migration of sand waves: The role of tidal forcing, sediment size and bed slope effects. *Continental Shelf Research*, 190, 103986. <https://doi.org/10.1016/j.csr.2019.103986>
- Wells, J. T., & Kim, S. Y. (1989). Sedimentation in the Albemarle-Pamlico lagoonal system: Synthesis and hypotheses. *Marine Geology*, 88(3–4), 263–284. [https://doi.org/10.1016/0025-3227\(89\)90101-1](https://doi.org/10.1016/0025-3227(89)90101-1)
- Westoby, M. J., Brasington, J., Glasser, N. F., Hambrey, M. J., & Reynolds, J. M. (2012). “Structure-from-Motion” photogrammetry: A low-cost, effective tool for geoscience applications. *Geomorphology*, 179, 300–314. <https://doi.org/10.1016/j.geomorph.2012.08.021>
- Wilcock, P. R., & DeTemple, B. T. (2005). Persistence of armor layers in gravel-bed streams. *Geophysical Research Letters*, 32(8), 1–4. <https://doi.org/10.1029/2004GL021772>

- Wilson, M. F. J., O'Connell, B., Brown, C., Guinan, J. C., & Grehan, A. J. (2007). Multiscale terrain analysis of multibeam bathymetry data for habitat mapping on the continental slope. *Marine Geodesy*, 30(1–2), 3–35. <https://doi.org/10.1080/01490410701295962>
- Witbaard, R., Bergman, M. J. N., van Weerlee, E., & Duineveld, G. C. A. (2017). An estimation of the effects of *Ensis directus* on the transport and burial of silt in the near-shore Dutch coastal zone of the North Sea. *Journal of Sea Research*, 127, 95–104. <https://doi.org/10.1016/j.seares.2016.12.001>
- Witbaard, R., Duineveld, G. C. A., Bergman, M. J. N., Witte, H. I. J., Groot, L., & Rozemeijer, M. J. C. (2015). The growth and dynamics of *Ensis directus* in the near-shore Dutch coastal zone of the North Sea. *Journal of Sea Research*, 95, 95–105. <https://doi.org/10.1016/j.seares.2014.09.008>
- Wong, M., & Parker, G. (2006). Reanalysis and correction of bed-load relation of Meyer-Peter and müller using their own database. *Journal of Hydraulic Engineering*, 132(11), 1159–1168. [https://doi.org/10.1061/\(asce\)0733-9429\(2006\)132:11\(1159\)](https://doi.org/10.1061/(asce)0733-9429(2006)132:11(1159))
- Xu, Y., Li, D., & Nepf, H. (2022). Sediment pickup rate in bare and vegetated channels. *Geophysical Research Letters*, 49(21), e2022GL101279. <https://doi.org/10.1029/2022GL101279>
- Yang, J. Q., Chung, H., & Nepf, H. M. (2016). The onset of sediment transport in vegetated channels predicted by turbulent kinetic energy. *Geophysical Research Letters*, 43(21), 11261–11268. <https://doi.org/10.1002/2016GL071092>
- Yang, J. Q., & Nepf, H. M. (2018). A turbulence-based bed-load transport model for bare and vegetated channels. *Geophysical Research Letters*, 45(19), 10428–10436. <https://doi.org/10.1029/2018GL079319>
- Zhao, T., & Nepf, H. M. (2021). Turbulence dictates bedload transport in vegetated channels without dependence on stem diameter and arrangement. *Geophysical Research Letters*, 48(21), e2021GL095316. <https://doi.org/10.1029/2021GL095316>